Robotica (2019) volume 37, pp. 1120–1142. © Cambridge University Press 2019
doi:10.1017/S0263574718001492

Approximate Stiffness Modelling and Stiffness Defect Identification for a Heavy-load Parallel Manipulator

Shuai Fan, Shouwen Fan*

School of Mechanical and Electrical Engineering, University of Electronic Science and Technology of China, Chengdu, Sichuan 611731, People's Republic of China. E-mail: fansuai12345@163.com

(Accepted December 20, 2018. First published online: February 18, 2019)

SUMMARY
When using parallel manipulators as machine tools, their stiffness is an important factor in the quality of the produced products. This paper presents an overall approximate stiffness model for a heavy-load parallel manipulator, which considers the effects of actuator stiffness, joint clearance, joint contact deformation, and limb deformation. Based on the principle of virtual work and the introduced modified parameters, the proposed overall compliance matrix successfully takes four factors into a unified expression. To obtain the overall compliance matrix, the approximate stiffness models of the joint clearance, joint contact deformation, and limb deformation are given. In addition, by combining the statistical simulation including the random uncertainties and the proposed approximate stiffness models as the basis of the magnitudes for each random variable, an approach based on the expected trajectory and external load is also proposed for stiffness defect identification such that the estimation is more accurate and reliable. Finally, a numerical example of the 1PU+3UPS parallel manipulator and a discussion are presented to demonstrate the practicability of the proposed stiffness model and defect identification approach. After modifying the structure parameters of the defective components, the prototype experiences a significant stiffness improvement.

KEYWORDS: Stiffness model; Overall compliance matrix; Defect identification; Parallel manipulator; Statistical simulation.

1. Introduction

Due to such advantages as greater load capacity, higher accuracy, and better ability to machine irregular surfaces, the use of parallel manipulators as machine tools has been favoured by many scholars. However, parallel manipulators for machining have not been widely used or marketed. An important reason for this is that their advantageous stiffness has not been highlighted compared with traditional machine tools.[1–3] As shown in Fig. 1, although the stiffness performance is taken into account in the design of the heavy-load parallel manipulator, the quality of the products is still unacceptable in the practical application of our prototype, as shown in Fig. 2. One of the reasons is that the stiffness model used is not accurate; therefore, a suitable stiffness model and a credible stiffness defect identification approach will be discussed in this paper.

In general, the stiffness is mainly represented by the stiffness matrix (the reciprocal of which is the compliance), which reveals the deformation relationship between the actuators and the moving platform.[4,5] However, the stiffness matrix only reflects the stiffness in the direction of degree of freedom (DOF) and assumes all components are ideal. For the aforementioned reasons, other factors are gradually considered in the stiffness model, such as limb deformation,[6–8] joint clearance,[9–11] joint contact deformation,[12–15] and others.[16] However, most models are a combination of two or three

* Corresponding author. E-mail: shouwenfan@263.net

https://doi.org/10.1017/S0263574718001492 Published online by Cambridge University Press

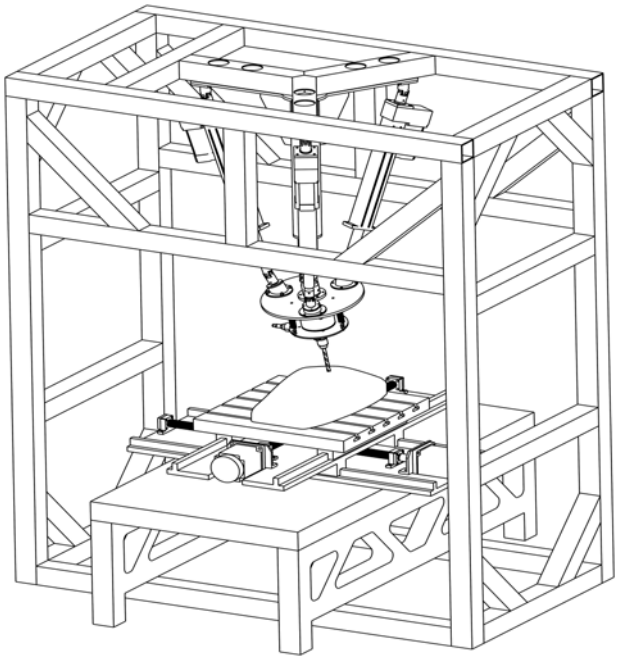


Fig. 1. 3D model of the parallel manipulator.

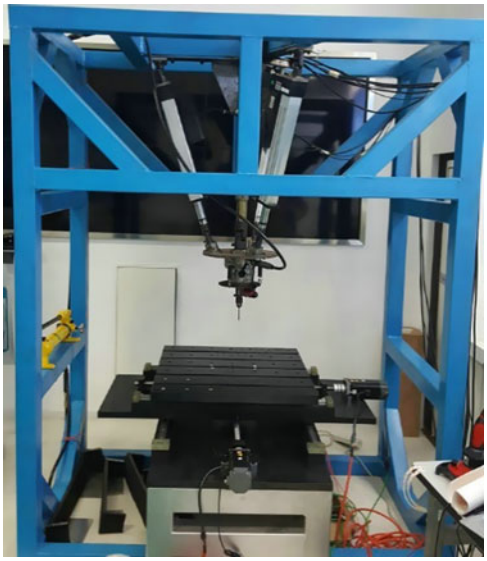


Fig. 2. Prototype of the parallel manipulator.

factors, such as actuator stiffness and limb deformation,[17,18] actuator stiffness and joint clearances,[19] joint clearances and limb deformation,[20,21] and others.[22,23] It can be seen that the previous studies focused on the partial factors, and there are few complete models. An important reason for this gap in the literature is that the theoretical foundations of these four factors are different; therefore, one of the purposes of this paper is to establish a systematic and unified stiffness model.

The clearances and contact deformation are major influences on the joints of the system, and these factors cannot be avoided due to their influences on such factors as assembly and elasticity.[12,24,25] The sophisticated mathematical models of the joint clearance have been extensively studied, and the parallel manipulator's deformation caused by joint clearances can be estimated based on these mathematical models.[9,10,26,27] In these studies, the estimations of the clearance's influences are expected to be as accurate as possible, but the reliability of the approximate stiffness is not considered. To solve the joint contact deformations, the most popular solution is to construct an elastic-damping contact

https://doi.org/10.1017/S0263574718001492 Published online by Cambridge University Press

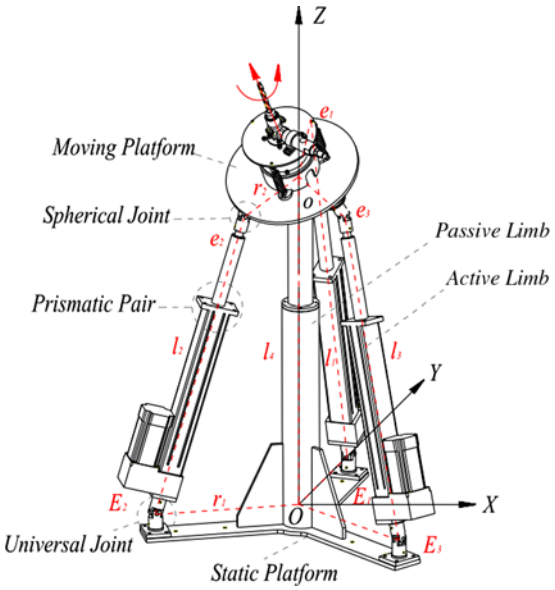


Fig. 3. 3D model of the 1PU+3UPS parallel manipulator.

force model, where the contact velocity is considered and the Hertzian Contact theory is utilized.[12,15] However, only the revolute joint has been studied in detail. Therefore, in response to the mentioned reasons, creating reliable approximate stiffness models and accurate contact models of the common joints are another purpose of this paper. Meanwhile, due to its practicality and concision,[28,29] the virtual work principle is utilized in this paper for the analysis of limb deformations, which can be a component of the systematic and unified stiffness model.

For the stiffness defect analysis, three mathematical tools were mainly used, including the vector and matrix technique,[4,5,26,30] the numerical method,[31–33] and the statistical method.[34,35] The first method needs to build a complete and accurate mathematical model of each component such that in many cases, only partial factors that affect the stiffness are analysed. Due to the uncertainty and complexity of the mathematical models of some of the components, the numerical analysis and statistical method were proposed. Compared with the first method, the numerical analysis and statistical method would result in confused results with uncontrollable factors, such as the worst case approach,[36] first-order second moment (FOSM),[34] method, and Monte Carlo method. However, the difference between the result and the actual is large for the worst case method, and the derivation of the FOSM method including the derivation is not applicable to the case where the number of variables is particularly large (in the stiffness analysis of this paper, there are up to 61 variables). Therefore, by combining the advantages of these methods, a hybrid method is proposed to identify the stiffness defect, in which the approximate stiffness model is analysed by the vector and matrix technique, and statistical simulation based on Monte Carlo method is used to take into account uncontrollable factors.

The main purpose of this paper is to estimate whether the selected component stiffness meets the design requirements and identify the factors that cause insufficient stiffness. The remainder of this paper is organized as follows. The architecture description and the statistical analysis of a 1PU+3UPS parallel manipulator are first given in Section 2. An overall stiffness model is presented in Section 3, and the defect identification method is proposed in Section 4. Next, a numerical example and a discussion are presented in Section 5. Finally, the study's conclusions are presented in Section 6.

2. Architecture and Statics

As shown in Fig. 3, the heavy-load parallel manipulator is a 1PU+3UPS structure (changing the UP limb of the Tricept robot to a PU limb), and the moving platform parallel manipulator is connected to the static platform by three uniformly distributed active limbs (UPS) and one passive limb (PU). The three active limbs are connected with the moving platform through three spherical joints and connected with the static platform through three universal joints. The passive limb is connected with the fixed platform through a prismatic pair and connected with the moving platform through a universal joint. Meanwhile, an absolute coordinate system of *O-XYZ* is fixed on the static platform,

https://doi.org/10.1017/S0263574718001492 Published online by Cambridge University Press

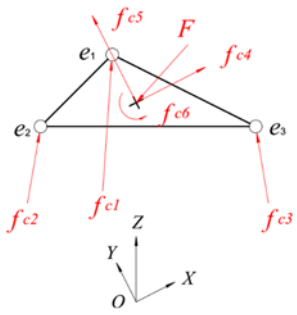


Fig. 4. Statics of moving platform.

and the position vectors of the universal joints and spherical joints are denoted by $\boldsymbol{e}_1$, $\boldsymbol{e}_2$, $\boldsymbol{e}_3$, $\boldsymbol{E}_1$, $\boldsymbol{E}_2$, and $\boldsymbol{E}_3$, respectively. Note that the three components of each three-dimensional vector are denoted by the symbol with the subscripts x, y, and z, such as $\boldsymbol{e}_1 = (e_{1x}, e_{1y}, e_{1z})$, and these notations are also applied in the later discussion.

Referring the Ref. [37], the moving platform possesses two rotational freedoms around the *Y-axis* and *X-axis*, and one translational freedom along the *Z-axis*. If an external wrench $\boldsymbol{F}$ acting on the centre of the moving platform, the constraint force of the moving platform can be easily solved by the screw method. As shown in Fig. 4, if gravity is ignored, the three driving limbs of the 1PU+3UPS parallel manipulator are only constrained by the pure force along their axial (denoted by f_{c1}, f_{c2}, and f_{c3}), and the constraint of the passive limb is a coupling of two forces (denoted by f_{c4} and f_{c5}) and a moment (denoted by f_{c6}), so the constraint equilibrium equations can be expressed as

$$\begin{cases} l_{1x}f_{c1} + l_{2x}f_{c2} + l_{3x}f_{c3} + f_{c4} = F_X \\ l_{1y}f_{c1} + l_{2y}f_{c2} + l_{3y}f_{c3} + f_{c5} = F_Y \\ l_{1z}f_{c1} + l_{2z}f_{c2} + l_{3z}f_{c3} = F_Z \\ [l_{1z}e_{1y} - l_{1y}(e_{1z} - l_4)]f_{c1} + [l_{2z}e_{2y} - l_{2y}(e_{2z} - l_4)]f_{c2} + [l_{3z}e_{3y} - l_{3y}(e_{3z} - l_4)]f_{c3} + f_{c4} = M_X \\ [l_{1x}(e_{1z} - l_4) - l_{1z}e_{1x}]f_{c1} + [l_{2x}(e_{2z} - l_4) - l_{2z}e_{2x}]f_{c2} + [l_{3x}(e_{3z} - l_4) - l_{3z}e_{3x}]f_{c3} + f_{c5} = M_Y \\ [l_{1y}e_{1x} - l_{1x}e_{1y}]f_{c1} + [l_{2y}e_{2x} - l_{2x}e_{2y}]f_{c2} + [l_{3y}e_{3x} - l_{3x}e_{3y}]f_{c3} + f_{c6} = M_Z \end{cases} \tag{1}$$

It can be expressed by a matrix form as

$$\boldsymbol{F}_c = \boldsymbol{H}\boldsymbol{F}, \tag{2}$$

where $\boldsymbol{F} = [F_X, F_Y, F_Z; M_X, M_Y, M_Z]T$, $\boldsymbol{F}_c = [f_{c1}, f_{c2}, f_{c3}, f_{c4}, f_{c5}, f_{c6}]^T$,

$$\boldsymbol{H} = \begin{bmatrix} l_{1x} & l_{2x} & l_{3x} & 1\ 0\ 0 \\ l_{1y} & l_{2y} & l_{3y} & 0\ 1\ 0 \\ l_{1z} & l_{2z} & l_{3z} & 0\ 0\ 0 \\ l_{1z}e_{1y} - l_{1y}(e_{1z} - l_4) & l_{2z}e_{2y} - l_{2y}(e_{2z} - l_4) & l_{3z}e_{3y} - l_{3y}(e_{3z} - l_4) & 0\ 0\ 0 \\ l_{1x}(e_{1z} - l_4) - l_{1z}e_{1x} & l_{2x}(e_{2z} - l_4) - l_{2z}e_{2x} & l_{3x}(e_{3z} - l_4) - l_{3z}e_{3x} & 0\ 0\ 0 \\ l_{1y}e_{1x} - l_{1x}e_{1y} & l_{2y}e_{2x} - l_{2x}e_{2y} & l_{3y}e_{3x} - l_{3x}e_{3y} & 0\ 0\ 1 \end{bmatrix}^{-1},$$

and

$$(l_{ix}, l_{iy}, l_{iz})^T = \frac{\boldsymbol{e}_i - \boldsymbol{E}_i}{|\boldsymbol{e}_i - \boldsymbol{E}_i|}.$$

3. Approximate Stiffness Model of the 1PU+3UPS Parallel Manipulator

When the driving elements are locked, the activity of the moving platform should be lost. However, the moving platform is active in a tiny workspace due to the inevitable joint clearances, joint contact deformations, and slight limb deformations. Since the accurate mathematical models of different factors are very complicated and the stiffness magnitude is the main concern, the approximate model is mainly discussed based on the following assumptions:

(a) The stiffness model is an approximate value of the deformation.
(b) The moving platform is rigid.

https://doi.org/10.1017/S0263574718001492 Published online by Cambridge University Press

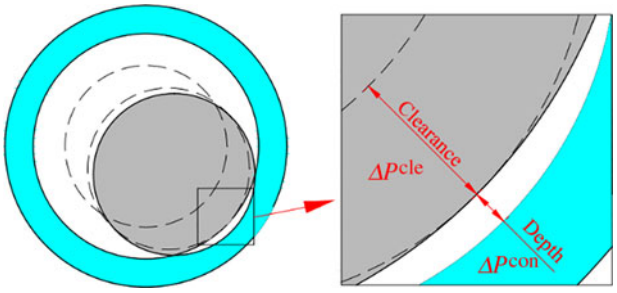


Fig. 5. Clearance and penetration depth of joints.

(c) The effects of the velocity of the moving platform can be ignored.
(d) The deformations caused by various factors are independent of each other.
(e) The effects of four factors can be regarded as a direct sum.

Therefore, the approximate tiny deformation of the moving platform can be defined as

$$\Delta \boldsymbol{P} = \Delta \boldsymbol{P}^{\text{act}} + \Delta \boldsymbol{P}^{\text{cle}} + \Delta \boldsymbol{P}^{\text{con}} + \Delta \boldsymbol{P}^{\text{def}}, \tag{3}$$

where $\Delta \boldsymbol{P}$ is the total tiny deformation of the moving platform, and $\Delta \boldsymbol{P}^{\text{act}}$, $\Delta \boldsymbol{P}^{\text{cle}}$, $\Delta \boldsymbol{P}^{\text{con}}$, and $\Delta \boldsymbol{P}^{\text{def}}$ are the tiny deformations caused by the actuator stiffness, joint clearances, joint contact deformations, and limb deformations, respectively. All the tiny deformations that are discussed later are composed of two three-dimensional vectors: $\Delta \boldsymbol{P} = [\Delta X, \Delta Y, \Delta Z; \Delta \Theta, \Delta \Phi, \Delta \Psi]^T$, where the first vector denotes the translation and the second vector denotes the rotation.

3.1. Approximate stiffness model of actuators

According to the force analysis, the three driving limbs of the 1PU+3UPS parallel manipulator are only constrained by the pure force along their axial. When the prismatic joint is the actuator of the heavy-load parallel manipulator, the electric cylinder that can only be subjected to axial force is frequently used, so the stiffness of actuators is axial and determined by the parameters of the produced electric cylinder. Therefore, if the joints are ideal and the limbs are rigid,[4] the tiny deformations of the moving platform caused by the stiffness of the actuators can be expressed as

$$\Delta \boldsymbol{P}^{\text{act}} = \boldsymbol{K}^{\text{act}} \boldsymbol{F}, \tag{4}$$

where $\boldsymbol{K}^{\text{act}}$ is the traditional compliance matrix of the parallel manipulators. Assuming that the stiffness of the three actuators which are axial are k_1, k_2, and k_3, the traditional compliance matrix can be obtained by

$$\boldsymbol{K}^{\text{act}} = \boldsymbol{J}_{6\times 3}\, \text{diag}\left(\frac{\mathbf{1}}{k_1}, \frac{\mathbf{1}}{k_2}, \frac{\mathbf{1}}{k_3}\right) \boldsymbol{H}_{3\times 6}, \tag{5}$$

where $\boldsymbol{J}_{6\times 3}$ is the Jacobian matrix which can be solved by taking the time derivative of constraint equations, and $H_{3\times 6}$ is the first three rows of the matrix $\boldsymbol{H}$.

3.2. Approximate stiffness model of joints

As shown in Fig. 5, the joint stiffness model consists of two parts: clearance and penetration depth. The stiffness models of clearance and penetration depth for the universal joint, revolute joint, prismatic pair, and spherical joint are defined in this section. Since the accurate mathematical models of the joint clearance and contact deformation are nonlinear and complexity, the presented models of this section are approximate stiffness models, where the stiffness along the directions of local coordinate axes is concerned.

3.2.1. Approximate clearance model of the universal joint. In most studies of universal joints, the clearances model is replaced by two revolute joints, but this approach introduces several unnecessary constraint parameters, and the amount of calculations will increase; therefore, a common class of

https://doi.org/10.1017/S0263574718001492 Published online by Cambridge University Press

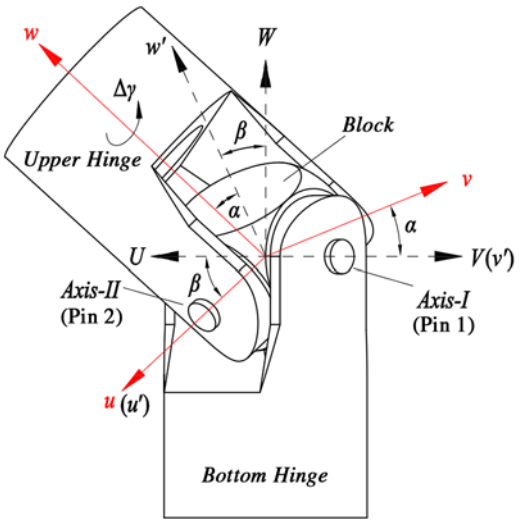


Fig. 6. 3D model of the universal joint.

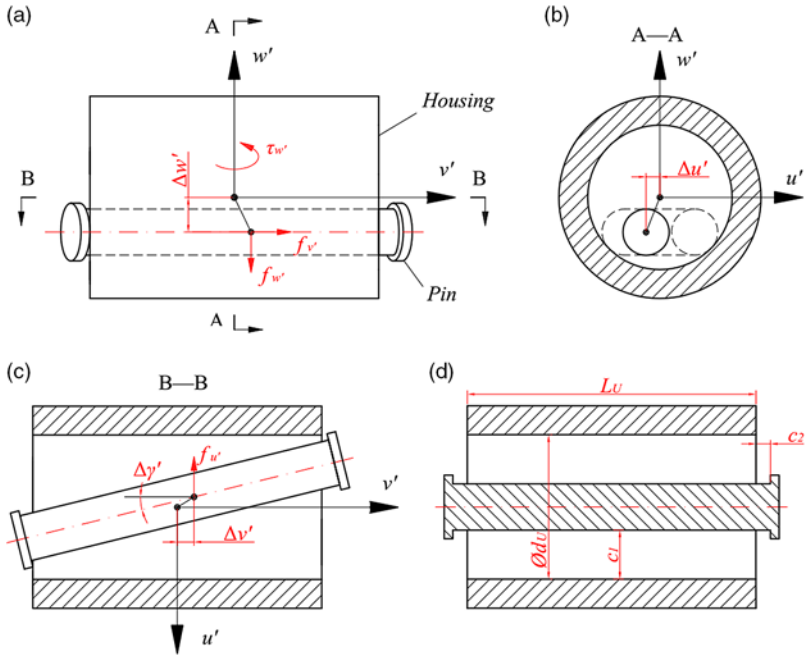


Fig. 7. Structure of a pin and housing: (a) *o-vw* plane, (b) *o-uw* plane, (c) *o-uv* plane, (d) parameters.

universal joint is fully studied in this section. As shown in Fig. 6, three coordinate systems are established in this section. The coordinate system *O-u'v'w'* is obtained by rotating the *O-UVW* coordinate system along its *V*-axis by β, and the coordinate system *O-uvw* (the local coordinate system, called LCS) is obtained by rotating the *O-u'v'w'* coordinate system along its *u'*-axis by α. Since the two rotating axes (Axis-I and Axis-II) of the two hinges are always orthogonal, the joint clearances will be discussed first in the *O-u'v'w'* system.

As shown in Fig. 6, the universal joint is composed of a bottom hinge, an upper hinge, and a cross trunnion that is made up of a block and two pins. Based on the first contact model for the revolute joints in Refs. [10, 27], the clearance model for a pin and a housing is established as shown in Fig. 7. Note that d_U and L_U are the internal diameter and the equivalent length of the housing, respectively, which depends on the actual structural parameters. When the constraint is a pure force, which can be decomposed into three components along three axes (*u'*-axis, *v'*-axis, and *w'*-axis), the clearances along three axes can be obtained. For example, in the *u'*-axis direction, the clearance is a sum of

https://doi.org/10.1017/S0263574718001492 Published online by Cambridge University Press

radial gap c_1 (between pin2 and upper hinge) and axial gap c_2(between pin1 and bottom hinge), where c_1 and c_2 are the values of the joint clearances shown in Fig. 7(d). Thus, the clearance model of this universal joint can be expressed by

$$(\Delta \boldsymbol{P}_U^{\text{cle}})' = [c_1 + c_2, c_1 + c_2, \mathbf{2}c_1, \mathbf{0}, \mathbf{0}, \mathbf{0}]^T. \tag{6}$$

Note that the assumption that the geometric interference only occurs between pins and hinges, and it means that the geometric interference will not occur between the lock of cross trunnion and two hinges. When the constraint is a pure moment, which is around the *w'*-axis, the constraint equation of the clearances is

$$d_U - \frac{d_U - \mathbf{2}c_1}{\cos(\Delta\gamma_{1U}^{\text{cle}})} = L_U \tan(\Delta\gamma_{1U}^{\text{cle}}). \tag{7}$$

Thus,

$$\Delta\gamma_{1U}^{\text{cle}} \approx \frac{-L_U + \sqrt{L_U^2 + \mathbf{4}d_U c_1}}{\mathbf{2}d_U}. \tag{8}$$

In this situation, the clearance model of this universal joint is

$$(\Delta \boldsymbol{P}_U^{\text{cle}})' = \left[\mathbf{0}, \mathbf{0}, \mathbf{0}, \mathbf{0}, \mathbf{0}, \frac{-L_U + \sqrt{L_U^2 + \mathbf{4}d_U c_1}}{d_U}\right]^T. \tag{9}$$

Therefore, the clearance model of the universal joint can be approximated by

$$(\Delta \boldsymbol{P}_U^{\text{cle}})' = \left[c_1 + c_2, c_1 + c_2, 2c_1, 0, 0, \frac{-L_U + \sqrt{L_U^2 + 4d_U c_1}}{d_U}\right]^T. \tag{10}$$

Finally, translating the results into the *O-uvw* coordinate system, the joint clearance is

$$\Delta \boldsymbol{P}_U^{\text{cle}} = \boldsymbol{R}_u(\alpha)(\Delta \boldsymbol{P}_U^{\text{cle}})', \tag{11}$$

where

$$\boldsymbol{R}_u(\alpha) = \begin{bmatrix} 1 & 0 & 0 & & & \\ 0 & \cos\alpha & -\sin\alpha & & \mathbf{0} & \\ 0 & \sin\alpha & \cos\alpha & & & \\ & & & 1 & 0 & 0 \\ & \mathbf{0} & & 0 & \cos\alpha & -\sin\alpha \\ & & & 0 & \sin\alpha & \cos\alpha \end{bmatrix}$$

3.2.2. Approximate clearance model of the combined spherical joint. In practical applications, the spherical joint is usually replaced by the combination of a revolute joint and a universal joint to obtain a larger workspace; therefore, a clearance model for the combined spherical joint is proposed. As shown in Fig. 8, if the *w*-axis of LCS is the rotation axis of the revolute joint, therefore, referring to the analysis of the universal joint, the clearance model of the combined spherical joint is established as

$$\Delta \boldsymbol{P}_S^{\text{cle}} = \Delta \boldsymbol{P}_U^{\text{cle}} + \Delta \boldsymbol{P}_R^{\text{cle}}. \tag{12}$$

Referring to Fig. 7, the clearance of the revolute joint is

$$\Delta \boldsymbol{P}_R^{\text{cle}} = \left[c_3, c_3, c_4, \frac{-L_R + \sqrt{L_R^2 + 4d_R c_3}}{2d_R}, \frac{-L_R + \sqrt{L_R^2 + 4d_R c_3}}{2d_R}, 0\right]^T, \tag{13}$$

https://doi.org/10.1017/S0263574718001492 Published online by Cambridge University Press

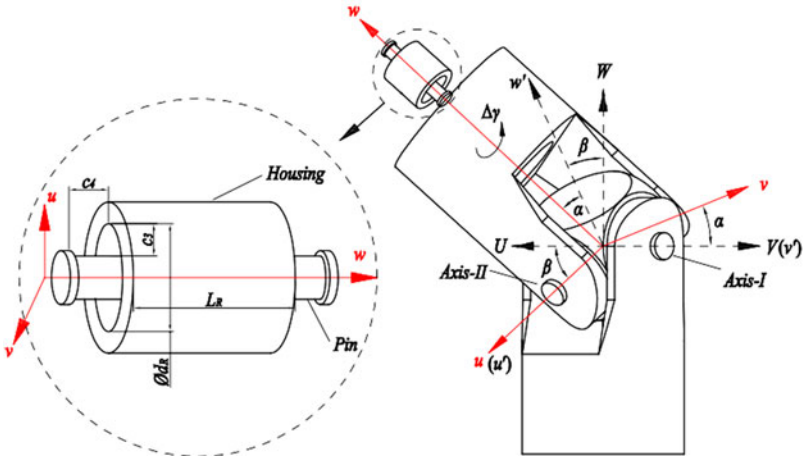


Fig. 8. 3D model of the combined spherical joint.

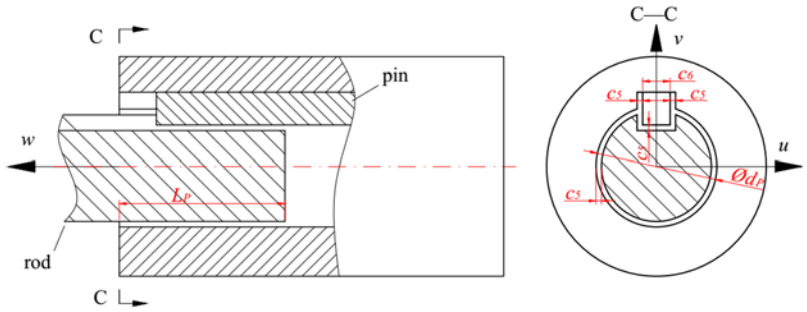


Fig. 9. Parameters of the prismatic pair.

where d_R and L_R are the internal diameter and the equivalent length of the revolute joint, respectively. Taking Eqs. (11) and (13) into Eq. (12), the clearance model of the combined spherical joint can be obtained.

3.2.3. Approximate clearance model of the prismatic pair. According to the defined parameters of the prismatic pair shown in Fig. 9, if the direction of translation is along the w-axis, the clearances models of the prismatic pair can be defined as

$$\Delta \boldsymbol{P}_P^{\text{cle}} = [\Delta u_P^{\text{cle}}, \Delta v_P^{\text{cle}}, \mathbf{0}, \Delta \alpha_P^{\text{cle}}, \Delta \beta_P^{\text{cle}}, \Delta \gamma_P^{\text{cle}}]^T. \tag{14}$$

Similarly, if the constraint is a pure force, the clearance model of this prismatic pair can be expressed by

$$\Delta \boldsymbol{P}_P^{\text{cle}} = [c_5, c_5, 0, 0, 0, 0, 0]^T. \tag{15}$$

If the constraint is a pure moment, the clearance model of this prismatic pair can be expressed by

$$\Delta \boldsymbol{P}_P^{\text{cle}} = [0, 0, 0, \Delta \alpha_P^{\text{cle}}, \Delta \beta_P^{\text{cle}}, \Delta \gamma_P^{\text{cle}}]^T, \tag{16}$$

where

$$\Delta \alpha_P^{\text{cle}} = \Delta \beta_P^{\text{cle}} = \frac{-L_P + \sqrt{L_P^2 + \mathbf{4} d_P c_5}}{\mathbf{2} d_P},$$

and

$$\Delta \gamma_P^{\text{cle}} = \arcsin\left(\frac{c_6 + \mathbf{2} c_5}{d_P - \mathbf{2} c_5}\right) - \arcsin\left(\frac{c_6}{d_P - \mathbf{2} c_5}\right) \approx \frac{\mathbf{2} c_5}{d_P - \mathbf{2} c_5}.$$

https://doi.org/10.1017/S0263574718001492 Published online by Cambridge University Press

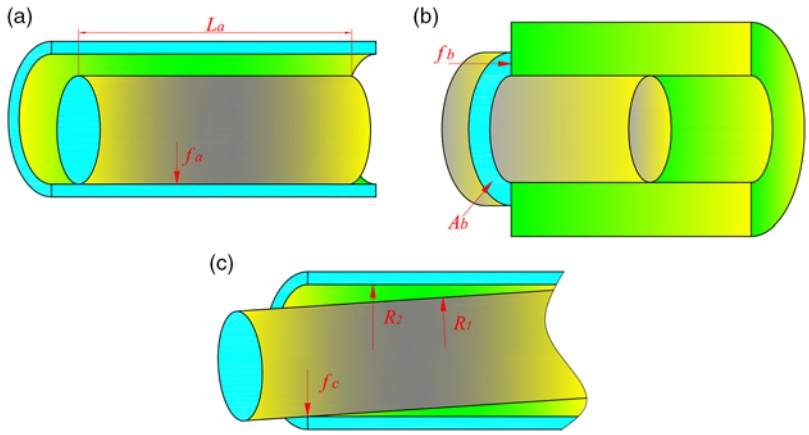


Fig. 10. Three contact models: (a) *model a,* (b) *model b*, (c) *model c*.

where d_P and L_P are the internal diameter and the equivalent length of the prismatic pair, respectively; therefore, the clearance model of the prismatic pair is a combination of the first two situations and is expressed as

$$\Delta \boldsymbol{P}_P^{\text{cle}} = \left[c_5,\, c_5,\, 0,\, \frac{-L_P + \sqrt{L_P^2 + 4d_P c_5}}{2d_P},\, \frac{-L_P + \sqrt{L_P^2 + 4d_P c_5}}{2d_P},\, \frac{2c_5}{d_P - 2c_5} \right]^T. \tag{17}$$

3.2.4. Approximate contact deformation models. During the machining, the reaction force in the joint is large; therefore, the tiny contact deformation of the joints cannot be ignored. In this section, the rigorous deformation model along the directions of local coordinate axes for the joints is presented under the solved constraint forces and moments (including the driving forces) using the Hertzian Contact theory.[38] Since the penetration depth is related to the contact surface, three useful contact models are given and shown in Fig. 10.

In Fig. 10(a), two contact bodies are cylindrical and their axes are parallel, so the contact force can be defined as

$$f_a = \frac{\pi}{4} E^* L_a d_a. \tag{18}$$

Therefore, the penetration depth can be expressed by

$$d_a = f_a k_a^{\text{con}},\ k_a^{\text{con}} = \frac{4}{\pi E^* L_a}, \tag{19}$$

where E^* is the modified moduli of the elasticity, L_a is the length of the contact portion, and d is the penetration depth or deformation along the contact force. If both bodies are elastic, the modified moduli E^* can be solved by

$$\frac{\mathbf{1}}{E^*} = \frac{\mathbf{1} - \nu_1^2}{E_1} + \frac{\mathbf{1} - \nu_2^2}{E_2}, \tag{20}$$

where E_1, E_2, ν_1, and ν_2 are the elastic modulus and Poisson's ratio of the two contact bodies, respectively, and this notation is also applicable in the following equations. As shown in Fig. 10(b), if the contact surfaces of the two contact bodies are parallel and the area of the contact surface denoted by A_b is known, the contact force is

$$f_b = \mathbf{2} E^* \sqrt{\frac{A_b}{\pi}} d. \tag{21}$$

Thus, the penetration depth is

$$d_b = f_b k_b^{\text{con}},\ k_b^{\text{con}} = \frac{\mathbf{1}}{\mathbf{2} E^*} \sqrt{\frac{\pi}{A_b}}. \tag{22}$$

https://doi.org/10.1017/S0263574718001492 Published online by Cambridge University Press

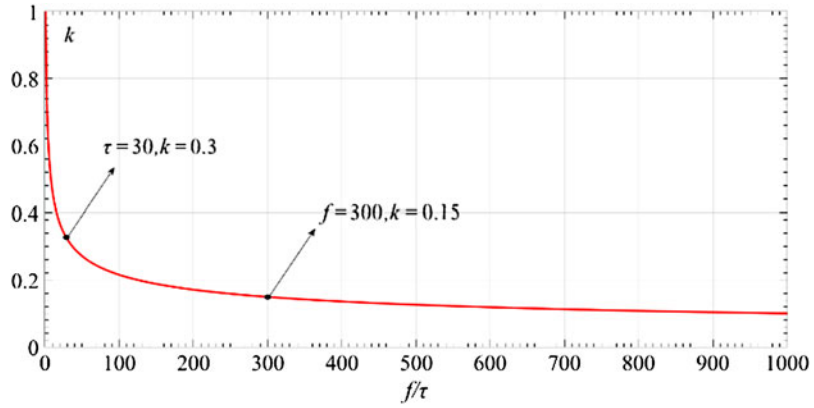


Fig. 11. Values of the modified parameter.

For the third contact model shown in Fig. 10(c), if the constraint is a moment, the contact force is

$$f_c = \frac{\tau_c}{L_c}, \tag{23}$$

and the contact force can be expressed as

$$f_c = \frac{4}{3} E^* R^{1/2} d_c^{3/2}, \tag{24}$$

where R is the equivalent radius of the two contact bodies. Due to the small difference between radius R_1 and radius R_2, the equivalent radius of the third model is

$$R = \sqrt{R_1 R_2}, \tag{25}$$

therefore, the penetration depth is

$$\theta_c = \frac{d_c}{L_c} = \frac{1}{L_c} \left(\frac{3\tau_c}{4 L_c E^* \sqrt{R}} \right)^{2/3}. \tag{26}$$

Furthermore, for the third contact model, the penetration depth can also be approximated as

$$\theta_c = \tau_c k_c^{\text{con}}, \; k_c^{\text{con}} = \frac{\delta}{L_c} \left(\frac{3}{4 L_c E^* \sqrt{R}} \right)^{2/3}, \tag{27}$$

where δ is a modified parameter, which can be determined using Fig. 11.

If the joints meet the following assumptions, the penetration depth vector can be computed easily using the four defined contact models:

(a) The reaction force is equal to the contact force and much greater than the friction.
(b) The joint deformation is linearly elastic and the contact velocity is ignored.
(c) The effects of the force and moment is not coupled.

Based on the mathematical model for joints shown in Figs. 4–7, the approximate contact deformation models for the universal joint, combined spherical joint, and prismatic pair can be defined as

$$\begin{aligned} \Delta \boldsymbol{P}_U^{\text{con}} &= \boldsymbol{R}_u(\alpha) \Delta \boldsymbol{k}_U^{\text{con}} \boldsymbol{R}_u'(\alpha) \boldsymbol{f}_c, \\ \Delta \boldsymbol{P}_S^{\text{con}} &= \Delta \boldsymbol{k}_R^{\text{con}} \boldsymbol{f}_c + \Delta \boldsymbol{P}_U^{\text{con}}, \\ \Delta \boldsymbol{P}_P^{\text{con}} &= \Delta \boldsymbol{k}_P^{\text{con}} \boldsymbol{f}_c, \end{aligned} \tag{28}$$

https://doi.org/10.1017/S0263574718001492 Published online by Cambridge University Press

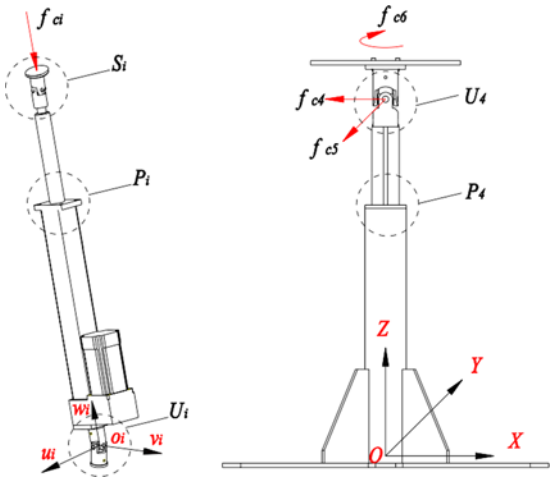


Fig. 12. Force analysis of limbs.

where

$$\Delta \boldsymbol{k}_U^{\text{con}} = [(k_a^{\text{con}} + k_b^{\text{con}}),\ (k_a^{\text{con}} + k_b^{\text{con}}),\ 2k_a^{\text{con}},\ 0,\ 0,\ 2k_c^{\text{con}}]^T,$$

$$\Delta \boldsymbol{k}_R^{\text{con}} = [k_a^{\text{con}},\ k_a^{\text{con}},\ k_b^{\text{con}},\ k_c^{\text{con}},k_c^{\text{con}},\ 0]^T,$$

$$\Delta \boldsymbol{k}_P^{\text{con}} = [k_a^{\text{con}},\ k_a^{\text{con}},\ 0,\ k_c^{\text{con}},\ k_c^{\text{con}},k_a^{\text{con}}]^T,$$

$$\boldsymbol{R}_u'(\alpha) = \begin{bmatrix} \mathbf{1} & \mathbf{0} & \mathbf{0} & & & \\ \mathbf{0} & \cos\alpha & \sin\alpha & & & \\ \mathbf{0} & -\sin\alpha & \cos\alpha & & & \\ & & & \mathbf{1} & \mathbf{0} & \mathbf{0} \\ & & & \mathbf{0} & \cos\alpha & \sin\alpha \\ & & & \mathbf{0} & -\sin\alpha & \cos\alpha \end{bmatrix}.$$

Taking the universal joint as an instance, the constraint is $\boldsymbol{f}_c$ expressed in the *o-uvw* coordinate system, and it can be translated to *o-u′v′w′* coordinate system $\boldsymbol{R}_u'(\alpha)\boldsymbol{f}_c$, which is decomposed into three pure forces along three coordinate axes (u'-axis, v'-axis, and w'-axis) and three pure moment around three coordinate axes (u'-axis, v'-axis, and w'-axis). Thus, the contact model along the u'-axis is the combination of *model a* (between pin 2 and upper hinge) and *model b* (between pin 1 and bottom hinge); the contact model along the v'-axis is the combination of *model a* (between pin 1 and bottom hinge) and *model b* (between pin 2 and upper hinge); the contact model along the w'-axis is double of *model a*; the contact model around the w'-axis is double of *model c*. As a result, the contact model of the universal joint can be obtained by $\boldsymbol{k}_U^{con}\boldsymbol{R}_u'(\alpha)\boldsymbol{f}_c$. Translating it to the *o-uvw* coordinate system, the contact deformation models for the universal joint are obtained.

3.2.5. Approximate stiffness model. The stiffness of parallel manipulators can be solved by the reaction force and principle of virtual work.[9,27] If the limb deformations and tangential friction are ignored and the reaction force is much greater than gravity, the contact force of the joints is approximately equal to the reaction force. According to the static analysis and the result in Fig. 12, when the rigid moving platform is subjected to a heavy external load and the actuators are locked, the equation for the virtual work principle can be expressed by

$$\begin{aligned}(\Delta \boldsymbol{P}^{cle} + \Delta \boldsymbol{P}^{con})^T \boldsymbol{F} + \sum_{i=1}^{3}[(\Delta \boldsymbol{P}_{Ui}^{cle} + \Delta \boldsymbol{P}_{Pi}^{cle} + \Delta \boldsymbol{P}_{Si}^{cle} + \Delta \boldsymbol{P}_{Ui}^{con} + \Delta \boldsymbol{P}_{Pi}^{con} + \Delta \boldsymbol{P}_{Si}^{con})^T \boldsymbol{f}_{ci}] \\ + \sum_{i=4}^{6}[(\Delta \boldsymbol{P}_{U4}^{cle} + \Delta \boldsymbol{P}_{P4}^{cle} + \Delta \boldsymbol{P}_{U4}^{con} + \Delta \boldsymbol{P}_{P4}^{con})^T \boldsymbol{f}_{ci}] = 0\end{aligned}, \tag{29}$$

where $\Delta \boldsymbol{P}_{Ui}^{cle}$, $\Delta \boldsymbol{P}_{Pi}^{cle}$, $\Delta \boldsymbol{P}_{Si}^{cle}$, $\Delta \boldsymbol{P}_{Ui}^{con}$, $\Delta \boldsymbol{P}_{Pi}^{con}$, and $\Delta \boldsymbol{P}_{Si}^{con}$ are clearance models and penetration depth models of the universal joint, prismatic pair, and spherical joint, respectively, $\boldsymbol{f}_{\text{ci}}$ is the reacting constraint wrench, and all of them are expressed in the LCS. Taking the results of statics and the previous

https://doi.org/10.1017/S0263574718001492 Published online by Cambridge University Press

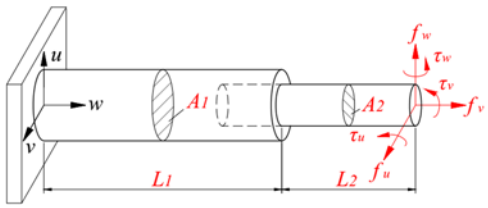


Fig. 13. 3D model of a limb.

clearance and contact deformation models for joints into Eq. (29), it can be expressed by a matrix form as

$$(\Delta \boldsymbol{P}^{\text{cle}} + \Delta \boldsymbol{P}^{\text{con}})^T \boldsymbol{F} = (\boldsymbol{K}^{\text{cle}} \boldsymbol{D}_1 + \boldsymbol{K}^{\text{con}} \boldsymbol{F}_c)^T \boldsymbol{H} \boldsymbol{F}. \tag{30}$$

Hence,

$$\Delta \boldsymbol{P}^{\text{cle}} + \Delta \boldsymbol{P}^{\text{con}} = \boldsymbol{H}^T (\boldsymbol{K}^{\text{cle}} \boldsymbol{D}_1 + \boldsymbol{K}^{\text{con}} \boldsymbol{F}_c), \tag{31}$$

where the matrixes $\boldsymbol{K}^{\text{cle}}$ and $\boldsymbol{K}^{\text{con}}$ are called the clearance and contact deformation compliance matrixes, respectively, and $\boldsymbol{D}_1$ is the direction vector. It is obvious that the direction vector is composed of two elements (1 and -1), and the elements are determined by the direction of the reaction force. If the amplitudes of the constraint wrench are not null, the direction vector can be solved by

$$\boldsymbol{D}_1 = \boldsymbol{D} \boldsymbol{F}_c, \tag{32}$$

where

$$\boldsymbol{D} = \text{diag}\left(\frac{\mathbf{1}}{|f_{c1}|}, \frac{\mathbf{1}}{|f_{c2}|}, \frac{\mathbf{1}}{|f_{c3}|}, \frac{\mathbf{1}}{|f_{c4}|}, \frac{\mathbf{1}}{|f_{c5}|}, \frac{\mathbf{1}}{|f_{c6}|} \right).$$

Taking Eqs. (2) and (32) into Eq. (31), the deformation caused by joints can be defined as

$$\Delta \boldsymbol{P}^{\text{cle}} + \Delta \boldsymbol{P}^{\text{con}} = \boldsymbol{H}^T \boldsymbol{K}^{\text{cle}} \boldsymbol{D} \boldsymbol{H} \boldsymbol{F} + \boldsymbol{H}^T \boldsymbol{K}^{\text{con}} \boldsymbol{H} \boldsymbol{F}, \tag{33}$$

In addition, the compliance matrixes $\boldsymbol{K}^{\text{cle}}$ and $\boldsymbol{K}^{\text{con}}$ can be expressed as

$$\begin{aligned} \boldsymbol{K}^{\text{cle}} &= \text{diag}(k_1^{\text{cle}}, k_2^{\text{cle}}, k_3^{\text{cle}}, k_4^{\text{cle}}, k_5^{\text{cle}}, k_6^{\text{cle}}), \\ \boldsymbol{K}^{\text{con}} &= \text{diag}(k_1^{\text{con}}, k_2^{\text{con}}, k_3^{\text{con}}, k_4^{\text{con}}, k_5^{\text{con}}, k_6^{\text{con}}), \end{aligned} \tag{34}$$

where

$$\begin{aligned} k_i^{\text{cle}} &= \Delta w_{Ui}^{\text{cle}} + \Delta w_{Si}^{\text{cle}} (i = 1, 2, 3), k_4^{\text{cle}} = \Delta u_{U4}^{\text{cle}} + \Delta u_{P4}^{\text{cle}}, k_5^{\text{cle}} \\ &= \Delta v_{U4}^{\text{cle}} + \Delta v_{P4}^{\text{cle}}, k_6^{\text{cle}} = \Delta \gamma_{U4}^{\text{cle}} + \Delta \gamma_{P4}^{\text{cle}}, \\ k_i^{\text{con}} &= \Delta w_{Ui}^{\text{con}} + \Delta w_{Si}^{\text{con}} (i = 1, 2, 3), k_4^{\text{con}} = \Delta u_{U4}^{\text{con}} + \Delta u_{P4}^{\text{con}}, k_5^{\text{con}} \\ &= \Delta v_{U4}^{\text{con}} + \Delta v_{P4}^{\text{con}}, k_6^{\text{con}} = \Delta \gamma_{U4}^{\text{con}} + \Delta \gamma_{P4}^{\text{con}}. \end{aligned}$$

Δu_{Ui}^{cle} is the clearance of ith universal joint in the direction of u-axis, and ΔU_{Ui}^{con} is the penetration depth of ith universal joint in the direction of the u-axis. The values of Δw_{Ui}^{cle}, Δw_{Si}^{cle}, Δu_{Pi}^{cle}, Δv_{Pi}^{cle}, $\Delta \gamma_{Ui}^{cle}$, Δv_{Ui}^{con}, Δw_{Ui}^{con}, Δw_{Si}^{con}, Δu_{Pi}^{con}, Δv_{Pi}^{con}, and $\Delta \gamma_{Ui}^{con}$ are similar, and all of the parameters can be obtained by the mathematical models that were given in the previous sections. Note that the penetration depths Δu_{Ui}^{con}, Δv_{Ui}^{con}, Δw_{Ui}^{con}, Δw_{Si}^{con}, Δu_{Pi}^{con}, Δv_{Pi}^{con}, and $\Delta \gamma_{Ui}^{con}$ are obtained after removing the reaction force in the joint contact deformation models.

3.3. Approximate stiffness model of limbs

If all of the joints are ideal and all the limbs are elastic, the deformation of the limbs will have a significant effect on the stiffness of the parallel manipulators. In this section, the deformation of a commonly used limb is studied in detail. As shown in Figs. 13 and 14, under the solved constraint

https://doi.org/10.1017/S0263574718001492 Published online by Cambridge University Press

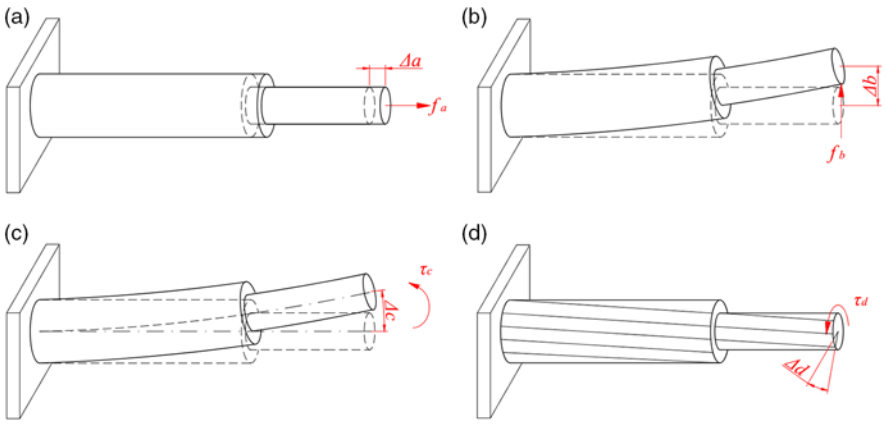


Fig. 14. Four deformation models: (a) model a, (b) model b, (c) model c, (d) model d.

forces and moments, four deformation models are discussed. Assuming that the deformations are linearly elastic and the moving platform is rigid, the deformations of the four deformation models are

$$(a)\Delta a = f_a k_a^{\text{def}},\ (b)\Delta b = f_b k_b^{\text{def}},\ (c)\Delta c = \tau_c k_c^{\text{def}},\ (d)\Delta d = \tau_d k_d^{\text{def}}, \tag{35}$$

where

$$k_a^{\text{def}} = \frac{L_1}{A_1 E} + \frac{L_2}{A_2 E},\ k_b^{\text{def}} = \frac{L_1^3}{3EI_1} + \frac{L_2^3 + 3L_1L_2(L_1 + L_2)}{3EI_2},$$
$$k_c^{\text{def}} = \frac{L_1}{EI_1} + \frac{L_2}{EI_2},\ k_d^{\text{def}} = \frac{L_1}{GJ_1} + \frac{L_2}{GJ_2}.$$

Let $\boldsymbol{I}$ denote the moment of inertia of the mandrel of the cross-section, and let $\boldsymbol{J}$ denote the moment of inertia of the centre of the circle. Then, the deformation model of the beam is

$$\Delta P_l^{\text{def}} = [f_u k_b^{\text{def}}, f_v k_a^{\text{def}}, f_w k_b^{\text{def}}, \tau_u k_c^{\text{def}}, \tau_v k_d^{\text{def}}, \tau_w k_c^{\text{def}}]^T. \tag{36}$$

Applying the same parameters to the joint stiffness model, the stiffness caused by limb deformation can be modelled as

$$(\Delta \boldsymbol{P}^{\text{def}})^T \boldsymbol{F} + \sum_{i=1}^{3} (\Delta \boldsymbol{P}_{li}^{\text{def}} \boldsymbol{f}_{ci}) + \Delta \boldsymbol{P}_{l4}^{\text{def}} (\boldsymbol{f}_{c4} + \boldsymbol{f}_{c5} + \boldsymbol{f}_{c6}) = 0. \tag{37}$$

Taking the beam deformation models into Eq. (37), the stiffness model can be redefined as

$$(\Delta \boldsymbol{P}^{\text{def}})^T \boldsymbol{F} = (\boldsymbol{K}^{\text{def}} \boldsymbol{F}_c)^T \boldsymbol{F}_c. \tag{38}$$

According to Eq. (2), it yields

$$(\Delta \boldsymbol{P}^{\text{def}})^T \boldsymbol{F} = (\boldsymbol{K}^{\text{def}} \boldsymbol{H} \boldsymbol{F})^T \boldsymbol{H} \boldsymbol{F}. \tag{39}$$

Thus,

$$\Delta \boldsymbol{P}^{\text{def}} = \boldsymbol{H}^T \boldsymbol{K}^{\text{def}} \boldsymbol{H} \boldsymbol{F}. \tag{40}$$

The corresponding matrix $\boldsymbol{K}^{\text{def}}$ is

$$\boldsymbol{K}^{\text{def}} = diag(k_1^{\text{def}}, k_2^{\text{def}}, k_3^{\text{def}}, k_4^{\text{def}}, k_5^{\text{def}}, k_6^{\text{def}}), \tag{41}$$

where

$$k_i^{\text{def}} = k_{ai}^{\text{def}} (i = 1, 2, 3),\ k_4^{\text{def}} = k_{b4}^{\text{def}},\ k_5^{\text{def}} = k_{b4}^{\text{def}},\ k_6^{\text{def}} = k_{d4}^{\text{def}}.$$

k_{ai}^{def} is the deformation parameter given in Eq. (35) of the ith limb, and the meanings of k_{bi}^{def} and k_{di}^{def} are similar.

https://doi.org/10.1017/S0263574718001492 Published online by Cambridge University Press

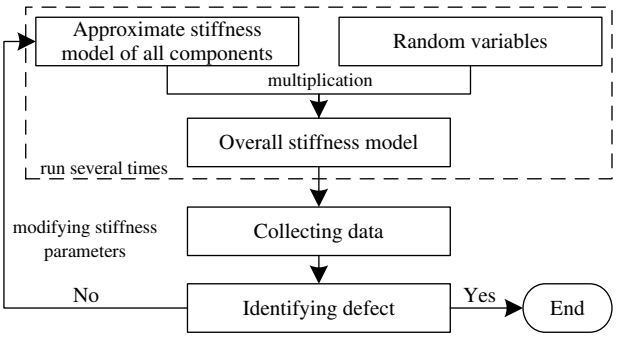


Fig. 15. Stiffness defect identification approach.

3.4. Overall approximate stiffness model

Taking Eqs. (4), (33), and (40) into Eq. (3) and writing it in a matrix form, the overall stiffness model can be defined by

$$\Delta \boldsymbol{P} = \boldsymbol{K}\boldsymbol{F}, \tag{42}$$

where the $\boldsymbol{K}$ is the overall compliance matrix, which is

$$\boldsymbol{K} = \boldsymbol{K}^{\text{act}} + \boldsymbol{H}^T\boldsymbol{K}^{\text{cle}}\boldsymbol{D}\boldsymbol{H} + \boldsymbol{H}^T\boldsymbol{K}^{\text{con}}\boldsymbol{H} + \boldsymbol{H}^T\boldsymbol{K}^{\text{def}}\boldsymbol{H}. \tag{43}$$

If the structural parameters of all components are given, the overall stiffness of any pose can be obtained.

4. Stiffness Defect Identification

After an external load is given and the actuators are locked, the moving platform can move with a tiny deformation in unknown directions, and the stiffness of the parallel manipulators can be revealed by this tiny deformation. In the introduced stiffness model, only an approximate value can be obtained, and it cannot accurately reflect the stiffness of the parallel manipulators. For example, it can be seen that the joint clearance model is controlled by the constraint force and moment. If the constraint is a pure force or moment, the clearance model is clear and easy to solve. However, if the constraint is a coupling of a force and moment, the clearance model is complicated, and the proposed clearance model will include several errors. Therefore, a statistical simulation tool is presented to predicate the stiffness.

The statistical simulation is a mathematical tool to solve the issues that impede the complicated calculations or impossible analytical solutions.[39] The core idea of this tool is to construct some certain regular random numbers and estimate the result based on probability statistics. As shown in Fig. 15, the defect identification approach is proposed based on the Monte Carlo method. In this approach, some independent normal distribution random variables are first generated, and then multiplying these random variables by approximate stiffness values of each components yields a statistical stiffness value of the parallel manipulator. After repeated operations and collecting data, the credible range of the stiffness value of the parallel manipulator can be obtained. If the result does not meet the requirements, the correction is made based on the percent contributions of each stiffness parameters.

4.1. Generating random variables

In the simulation model, the distribution of the generated random variables has a great influence on the results. After comparing some common distributions, the normal distribution of random variables is used based on the actual situation. If $\varepsilon_1, \varepsilon_2, \ldots, \varepsilon_{i+1}$ are independent standard random variables and uniformly distributed over the interval (0, 1), the variables of the standard normal distribution can be expressed as follows based on the Box-Muller transformations:

$$\chi_i = \sqrt{-2\log\varepsilon_i}\cos(2\pi\varepsilon_{i+1}),$$

$$\chi_{i+1} = \sqrt{-2\log\varepsilon_i}\sin(2\pi\varepsilon_{i+1}). \tag{44}$$

https://doi.org/10.1017/S0263574718001492 Published online by Cambridge University Press

Converting them to the general normal distribution with a mean μ_0 and variance σ, the results are

$$\chi_i = \mu_0 + \sigma\sqrt{-2\log\varepsilon_i}\cos(2\pi\varepsilon_{i+1}),\ \chi_{i+1} = \mu_0 + \sigma\sqrt{-2\log\varepsilon_i}\sin(2\pi\varepsilon_{i+1}). \tag{45}$$

4.2. Generating geometric variables including uncertainty effects

Since the approximate stiffness value in the stiffness model given in Section 3 is a scalar, the exact stiffness value is uncertain. Using the statistical simulation method, the statistical stiffness model can be obtained by multiplying the approximate stiffness value by a random variable, so that the statistical stiffness models of all joints and limbs can be determined. For example, according Eq. (17), a statistical stiffness model caused by the clearance of the prismatic pair can be defined by

$$\Delta \boldsymbol{P}_P^{\text{cle}} = [c_5\chi_1,\ c_5\chi_2,\ 0,\ \frac{-L_P + \sqrt{L_P^2 + 4d_P c_5}}{2d_P}\chi_3,\ \frac{-L_P + \sqrt{L_P^2 + 4d_P c_5}}{2d_P}\chi_4,\ \frac{2c_5}{d_P - 2c_5}\chi_5]^T. \tag{46}$$

where χ_1, χ_2, χ_3, χ_4, and χ_5 are five independent random variables. Obviously, the statistical stiffness value is uncertain and its distribution depends on the distribution of random variables. Therefore, the mean μ_0 and variance σ of the random variables are important. Since the stiffness value is greater than or equal to zero, the relationship between the mean and the variance of the normal distribution can be obtained based on the the 3σ theory (Pauta criterion):

$$\mu_0 - 3\sigma = 0. \tag{47}$$

Based on the previous relationship, Eq. (45) can be rewritten as

$$\chi_i = \mu_0 + \frac{\mu_0}{3}\sqrt{-2\log\varepsilon_i}\cos(2\pi\varepsilon_{i+1}),\ \chi_{i+1} = \mu_0 + \frac{\mu_0}{3}\sqrt{-2\log\varepsilon_i}\sin(2\pi\varepsilon_{i+1}). \tag{48}$$

It means the random χ_i is mainly distributed in interval $(\mu_0 - 3\sigma,\ \mu_0 + 3\sigma)$ or $(0,\ \mu_0 + 3\sigma)$; thus the statistical stiffness value $k_i\chi_i$ is mainly distributed in interval $(0,\ k_i(\mu_0+3\sigma))$, where the random uncertainty is included.

Clearly, the value of the mean μ_0 is very critical for uncertainty effects. According to the physical meaning of the approximate stiffness model, the suggested range of the mean is 0.5–1. The greater mean, the more reliable. For example, if the mean is equal to 1, the statistical stiffness value $k_i\chi_i$ is mainly distributed in interval $(0,\ 2k_i)$.

4.3. Collecting data

One simulation provides one independent result. If the simulation system is run several times, it will yield several results. By comparing these simulation results, we can reach a trustworthy result. If the quality of the simulation result is estimated by the mean, the sample mean is

$$\Delta \boldsymbol{P}_{\text{mea}} = \sum_{i=1}^{k}\left(\frac{\mathbf{1}}{k}\Delta \boldsymbol{P}_i\right). \tag{49}$$

Clearly, the mean value can be the optimal design or other valid solutions, but the simple mean value is not an accurate result. Hence, the confidence level and confidence intervals are introduced. According to the mean value and the estimated confidence level (90%) that can be adjusted according to the application, the confidence intervals are determined by the following steps: (a) taking the mean value as the middle value, the points closest to the mean value are in turn involved from the left and right, respectively, and the percentage of these points is calculated; (b) when the percentage of these points reaches to the confidence level, the confidence interval that is composed of the end points of the left and right can be determined; (c) the end points of the left and right are called the minimum and maximum values, respectively, so the confidence intervals are determined.

Therefore, the maximum and minimum values (the end points of the left and right) used as the basis of the accurate estimation can be obtained from the confidence intervals, and they are

$$\Delta \boldsymbol{P}_{\max} = \max(\Delta \boldsymbol{P}_1,\ \Delta \boldsymbol{P}_2,\ \cdots,\ \Delta \boldsymbol{P}_{run_times})$$

$$\Delta \boldsymbol{P}_{\min} = \min(\Delta \boldsymbol{P}_1,\ \Delta \boldsymbol{P}_2,\ \cdots,\ \Delta \boldsymbol{P}_{run_times}) \tag{50}$$

https://doi.org/10.1017/S0263574718001492 Published online by Cambridge University Press

Table I. Joint parameters and material properties.

c_1 (m)	c_2(m)	L_U(m)	$\phi\, d_U$ (m)	A_U(m^2)	c_3 (m)	c_4(m^2)	$\phi\, d_P$(m)
0.0001	0.0001	0.03	0.008	0.0001037	0.0001	0.05	0.035
Δ	c_5(m)	c_6 (m)	E (Gpa)	υ	G (Gpa)	A_1(m^2)	A_2 (m^2)
0.15	0.0001	0.0001	75	0.28	20	0.0079	0.0032

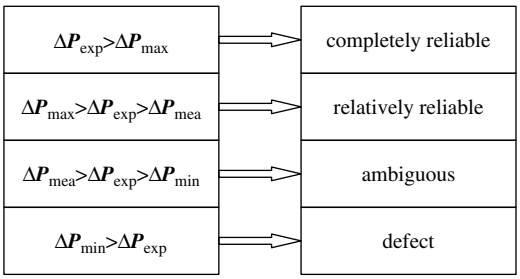


Fig. 16. Defect identification.

4.4. Identifying defect

Define the expected deformation (tolerant maximum deformation) as the expectation, denoted by $\Delta \boldsymbol{P}_{\text{exp}}$. Then, the reliability of the stiffness can be obtained by comparing the expectation and simulation results. As shown in Fig. 16, the reliability is divided into four levels: completely reliable, relatively reliable, ambiguous, and unreliable. If the $\Delta \boldsymbol{P}_{\text{exp}} > \Delta \boldsymbol{P}_{\text{max}}$, the deformation of the parallel manipulator meets the requirements and is without defects; if the $\Delta \boldsymbol{P}_{\text{max}} > \Delta \boldsymbol{P}_{\text{exp}} > \Delta \boldsymbol{P}_{\text{mean}}$, the reliability of the stiffness is relatively reliable and the stiffness of the parallel manipulator is satisfactory in most cases; if the $\Delta \boldsymbol{P}_{\text{mea}} > \Delta \boldsymbol{P}_{\text{exp}} > \Delta \boldsymbol{P}_{\text{min}}$, the stiffness may not meet the requirements and the machined product may not be qualified; if the $\Delta \boldsymbol{P}_{\text{min}} > \Delta \boldsymbol{P}_{\text{exp}}$, the designed parallel manipulator has a stiffness defect and it must be redesigned.

5. Numerical Example and Discussion

5.1. Numerical example

For the prototype of the 1PU+3UPS parallel manipulator in our laboratory, the length from geometrical centre of moving platform to the tip of tool is 0.312 m, and the radii of static platform and moving platform are 0.382 and 0.155 m, respectively. As shown in Table I, the joint structural parameters and material properties are given, where all universal joints, revolute joints, prismatic pairs, and their materials are same. In the workspace of the 1PU+3UPS parallel manipulator, the hypothetical trajectory of the tip of tool and the hypothetical external load acting on the tip of tool are given in Eq. (51), where t is the step size. Note that the local hypothetical trajectory at the edge of the dexterous workspace, where the stiffness is the weakest:

$$\begin{cases} X = 0.1\sin(\pi t) \\ Y = -0.1\cos(\pi t), \\ Z = 1 + 0.08t \end{cases} \begin{cases} F_X = -300\cos(\pi t) \\ F_Y = -300\sin(\pi t)\ . \\ F_Z = -500 \end{cases} \tag{51}$$

Assume that the three actuators have a stiffness of 2.5×10^8 N/m. Based on Eq. (4), the tiny deformation of the given trajectory caused by the actuator stiffness is shown in Fig. 17. By taking the structural parameters into Eqs. (33) and (40), the tiny deformations of the trajectory caused by joint clearances, joint contact deformations, and limb deformations can be obtained, as shown in Fig. 18. Finally, combining the previous results, the total tiny deformations can be obtained easily and are shown in Fig. 19.

Clearly, the obtained results are from the approximate stiffness estimation model. If this estimation model is adopted, the actual stiffness of the parallel manipulator may be unknown. Therefore, based on the defect identification method proposed in Section 4, 61 independent random numbers are introduced into the stiffness model, 3 of which are actuator stiffness, 26 of which are joint clearances, 26 of which are joint contact deformations, and the remaining of which are the limb deformations.

https://doi.org/10.1017/S0263574718001492 Published online by Cambridge University Press

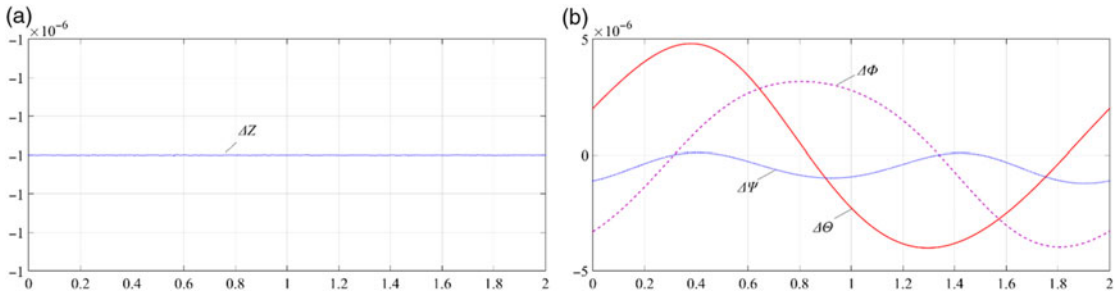


Fig. 17. Tiny deformations caused by the actuator stiffness: (a) translation; (b) rotation.

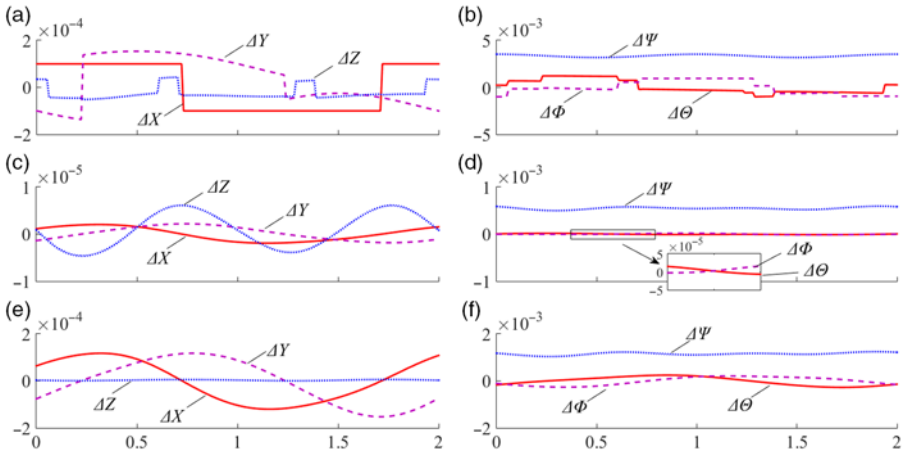


Fig. 18. Tiny deformations: (a) translation of joint clearances; (b) rotation of joint clearances; (c) translation of joint deformations; (d) rotation of joint deformations; (e) translation of limb deformations (f) rotation of limb deformations.

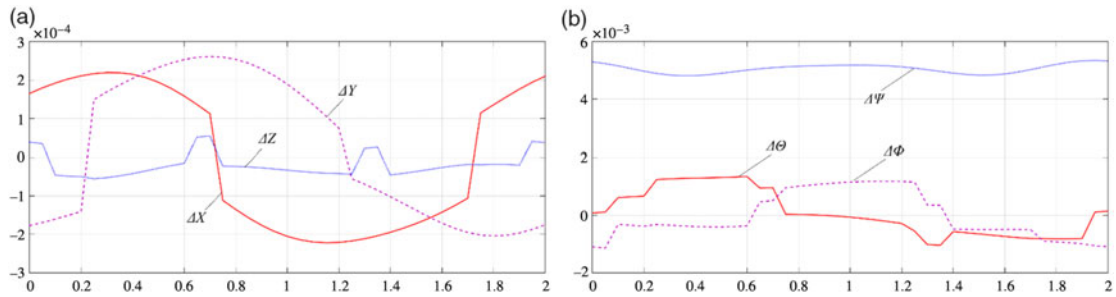


Fig. 19. Total tiny deformations: (a) translation; (b) rotation.

As shown in Fig. 20, when the given confidence level is 90% and the runtime is 1000, the minimum to maximum of the confidence intervals can be determined. Hence, the statistical model can be obtained and is shown in Fig. 21, where only the translational deformations are shown.

5.2. Comparisons of different effects

To verify the integrity of the proposed overall stiffness model, a case where the deformation of $\Delta\Phi$ is taken as a comparison is shown in Fig. 22, where the actuator stiffness and limb deformation are considered in Refs. [17, 18], the actuator stiffness and joint clearances are considered in Ref. [19], and the joint clearances and limb deformation are considered in Refs. [20, 21]. The results of Refs. [17, 18] in this numerical model are very similar to the model shown in this paper, but the results of Refs. [19–21] are different from those using the model in this paper. As shown in Fig. 23, the tiny deformation caused by the joint contact deformation and the actuator stiffness are small compared to the tiny deformation caused by the limb deformations and the joint clearances, and the difference

https://doi.org/10.1017/S0263574718001492 Published online by Cambridge University Press

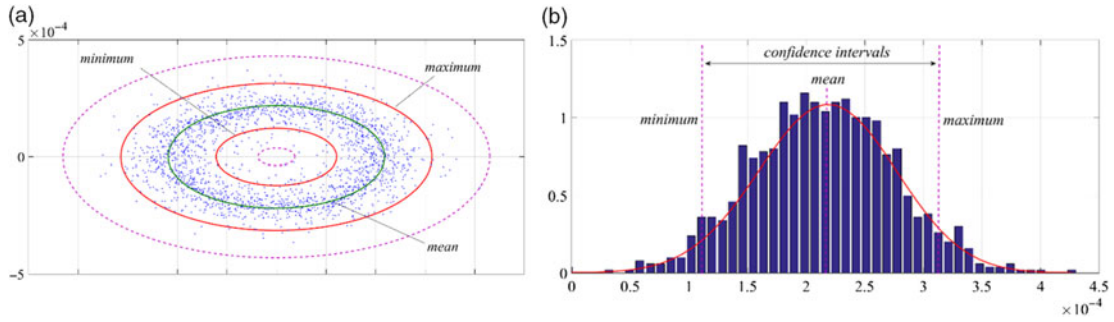


Fig. 20. Statistical deformation of ΔX for the point (0.0861, 0.0509, 1.026): (a) distribution; (b) probability distribution.

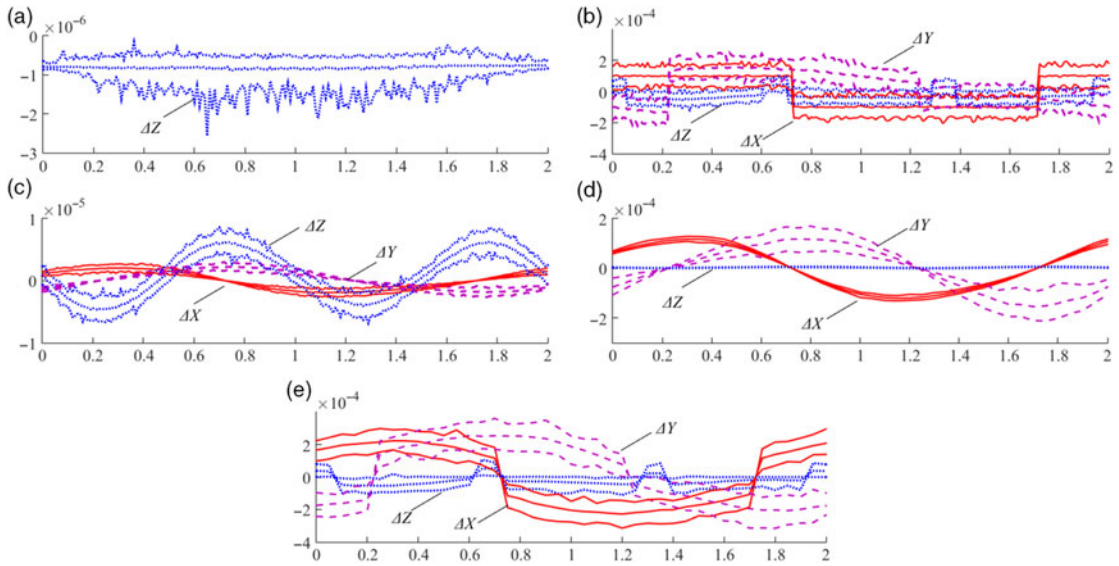


Fig. 21. Statistical deformation of translation for: (a) actuator; (b) joint clearance; (c): joint contact deformation; (d) limb deformation; (e): Total.

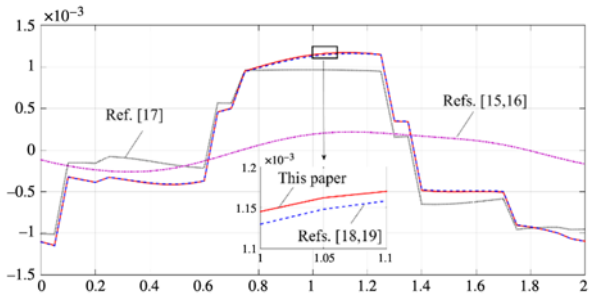


Fig. 22. Comparisons of $\Delta\Phi$ for different influence factors.

(about two orders of magnitude) is huge. A most important reason for this is that the actuator stiffness is estimated with better values in our numerical model. If the actuator stiffness decreases, the results described in Refs. [18,19] will be different from the results in this paper. In contrast, as joint accuracy increases and the external force decreases, the contribution to the overall deformation of the joint clearances and limb deformation will decrease, so the difference between these stiffness models also changes.

5.3. Comparisons of different approaches

To verify the advantage of the proposed estimation approach, the worst case approach[36] and the FOSM[34] method are compared. In the worst case approach, the stiffness variables take the maximum

https://doi.org/10.1017/S0263574718001492 Published online by Cambridge University Press

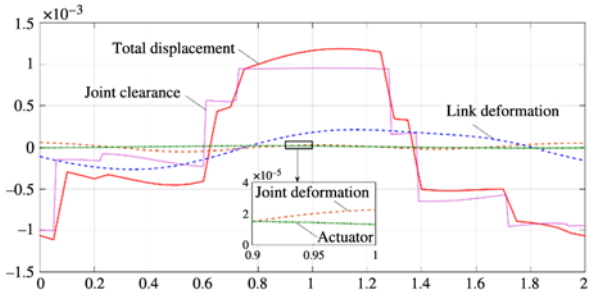


Fig. 23. Deformation of $\Delta\Phi$ for the numerical example.

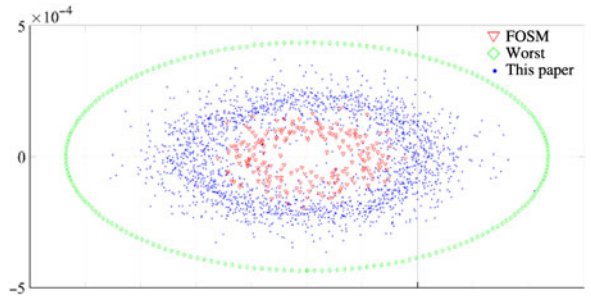


Fig. 24. Limb deformation of two methods.

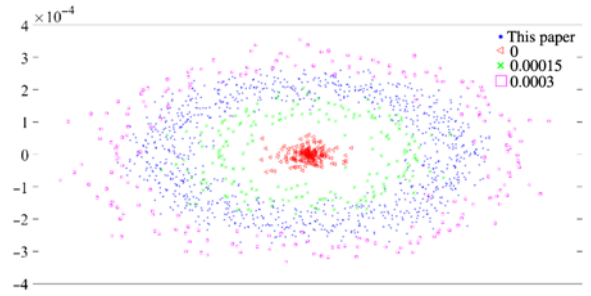


Fig. 25. Joint clearance of two methods.

value to obtain a tiny displacement of the mobile platform. As shown in Fig. 24, the results of the worst case approach are significantly larger than the other two methods. For the FOSM method, let the stiffness variables be $\boldsymbol{k} = (k_1, k_2, \ldots, k_{61})$ and their means be $\mu = (\mu_1, \mu_2, \ldots, \mu_{61})$, the tiny displacement of them can be defined as

$$\Delta P \approx P_{\text{act}}(\boldsymbol{\mu}) - P_{\text{req}} - \sum_{i=1}^{n} \frac{\partial P_{\text{act}}(\boldsymbol{k})}{\partial k_i} k_i, \tag{52}$$

where P_{act} and P_{req} are the actual output and required output, respectively. Obviously, the results obtained by the FOSM method are more concentrated than the results of this paper, but the process of derivation makes the FOSM method more complicated than the method in this paper due to the large number of variables. In addition, the results of the FOSM method are significantly affected by the required output, which is difficult to determine for the stiffness analysis. For example, taking the ΔX of the point (0.0861, 0.0509, 1.026)as the object, when the required output are 0, 0.15 and 0.3 mm, respectively, the results vary widely, as shown in Fig. 25. Consequently, the worst case approach and the FOSM method are not suitable for the stiffness analysis of this paper.

Furthermore, the results of the simulation by the software of Abaqus are presented for verifying the accuracy of the proposed model. The 3D model of the parallel manipulator at the point (-0.1, 0, 1.04) is shown in Fig. 26, where the model has been simplified and all clearances are equal to 0.1 mm. When the force continues to act for 5 s, the resulting displacement in the X-direction is shown in

https://doi.org/10.1017/S0263574718001492 Published online by Cambridge University Press

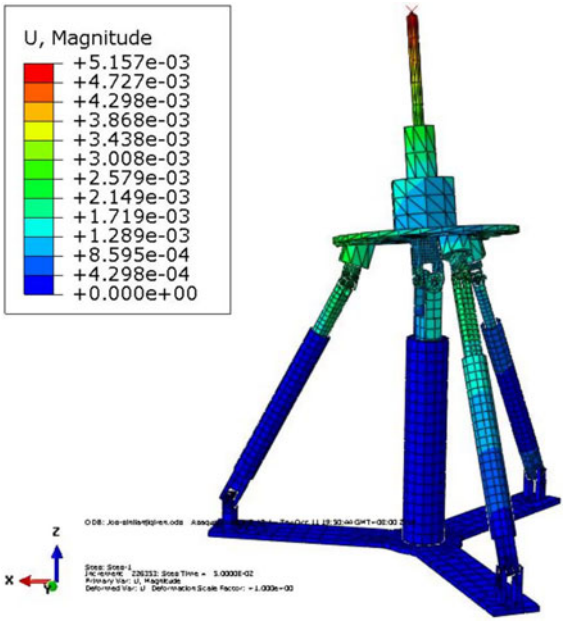


Fig. 26. 3D Model in the software of Abaqus.

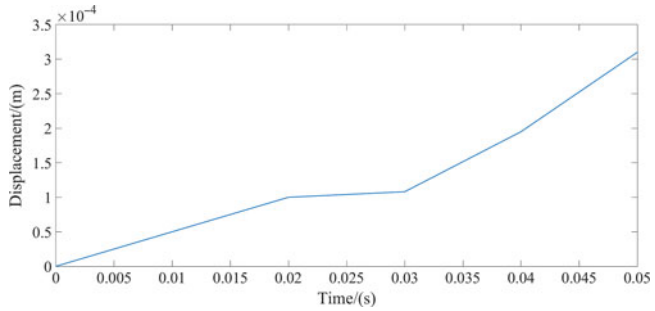


Fig. 27. Results by Abaqus for the point (-0.1, 0, 1.04).

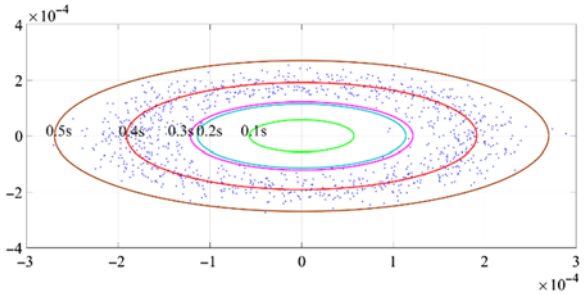


Fig. 28. Results of this paper and Abaqus.

Fig. 27. Clearly, the resulting displacement is local in the approximate range of this paper, as shown in Fig. 28, so the results of the Abaqus show that the proposed approximate stiffness model is correct and accuracy.

5.4. Stiffness defect identification

According to the defect identification approach, taking the *X*-direction as the research object, three tolerant deformations are given as 0.4, 0.25, and 0.1 mm. As shown in Fig. 29, if the expectation value is 0.4 mm, the numerical model can meet the requirements; if the expectation is 0.25 mm, some points in the trajectory may not reach the stiffness requirements; if the expectation is expected

https://doi.org/10.1017/S0263574718001492 Published online by Cambridge University Press

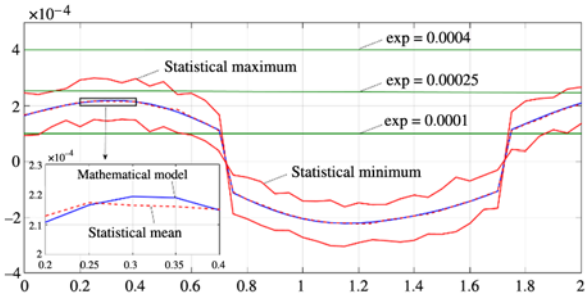


Fig. 29. Defect identification for ΔX.

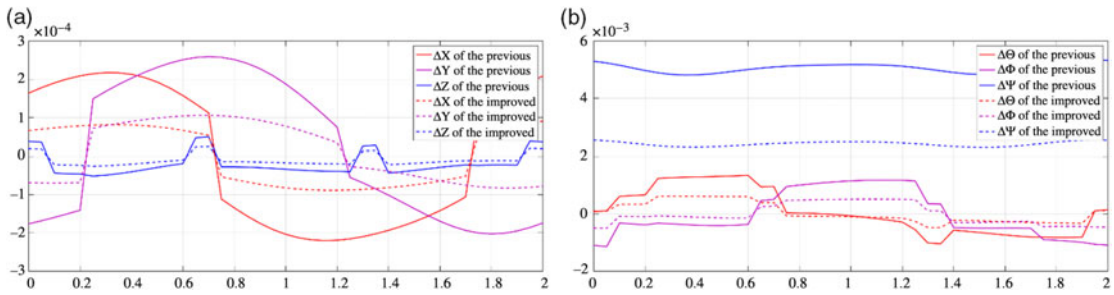


Fig. 30. Total tiny deformations of the improved model: (a) translation; (b) rotation.

to be 0.1 mm, it is clear that the stiffness of the machine is unknown. When the parameters need to be optimized or the parallel manipulator needs to be redesigned, the optimal direction can be found using our proposed overall approximate stiffness model.

5.5. Results

According to the discussions there are four clear results: (a) if only one single factor or partial factors are considered, it is clear that the stiffness model is very inaccurate; (b) the compliance matrix used in previous designs cannot precisely reflect the actual stiffness model; (c) for heavy-load but lower-DOF parallel manipulators, small deformations in the restraining direction cannot be ignored; (d) the mathematical estimation model is not accurate, but the statistical model provides a reliable stiffness model. Moreover, according to the results for numerical example of the 1PU+3UPS parallel manipulator, the stiffness performances of the prototype are clear, as (a) the stiffness along or around the X-axis and the Y-axis is approximately equal; (b) the stiffness along the Z-axis is greater than the stiffness along the X-axis and the Y-axis, but the rotation constraint around the Z-axis needs to be strengthened; and (c) the stiffness of the actuators is good, but the stiffness of the limbs should be strengthened and the joint clearances should be reduced.

For the identified stiffness defects, after studying the various factors and the contributions of each component, the joint clearances have been reduced from 0.1 to 0.05 mm and the strength of the passive PU limbs has been strengthened by increasing the diameter from 35 to 64 mm. As shown in Fig. 30, the deformations of the moving platform in the ΔX, ΔY, ΔZ, $\Delta\Theta$, $\Delta\Phi$, and $\Delta\Psi$ directions have been reduced by 63.6%, 59.2%, 54.2%, 55.3%, 56.7%, and 52%, respectively, so the stiffness improvement of the prototype is significant.

6. Conclusions

In this paper, the advantages of stiffness modelling can be summarized as follows: (a) the approximate contact deformation models of three common joints are given; (b) the proposed compliance matrix is independent of the external load; and (c) the proposed compliance matrix has unified the effects of actuator stiffness, joint clearance, joint contact deformation, and limb deformation. Meanwhile, the virtues of the stiffness defect identification method can be described as follows: (a) the uncontrollable and unsolvable factors that are involved; (b) the reliability of the statistical

https://doi.org/10.1017/S0263574718001492 Published online by Cambridge University Press

simulation is introduced; and (c) the stiffness weakness of the parallel manipulator can be found, and the corresponding direction of the optimization and improvement is clear.

However, in the approximate stiffness model, the exact models of all components of the parallel manipulator are needed; thus, the workload of this method is enormous. Because the effects of velocity are ignored, it is not applicable to certain parallel manipulators in which the effects of their moving velocity are important. In addition, this paper primarily discusses the defects from the contributions of the influencing factors for a specific parallel manipulator. In the future, the stiffness effects of the limbs and the joints on different structures will be investigated.

Funding

This work was supported by the National Natural Science Foundation of China under Grant 51175067 and 51875086.

References

1. J. P. Merlet, *Parallel Robots*, Second Edition (Springer, Netherlands, 2006).
2. Y. Shneor and V. T. Portman, "Stiffness of 5-axis machines with serial, parallel, and hybrid kinematics: Evaluation and comparison," *Annals-Manuf. Techn.* **59**(1), 409–412 (2010).
3. Z. Huang, Q. C. Li and H. F. Ding, *Theory of Parallel Mechanisms* (Springer, Netherlands, 2013).
4. B. S. El-Khasawneh and P. M. Ferreira, "Computation of stiffness and stiffness bounds for parallel link manipulators," *Int. J. Mach. Tools. Manuf.* **39**(2), 321–342 (1999).
5. G. Y. Huang, S. Guo, D. Zhang, H. B. Qu and H. Y. Tang, "Kinematic analysis and multi-objective optimization of a new reconfigurable parallel mechanism with high stiffness," *Robotica* **36**(2), 187–203 (2018).
6. G. Piras, W. L. Cleghorn and J. K. Mills, "Dynamic finite-element analysis of a planar high-speed, high-precision parallel manipulator with flexible links," *Mech. Mach. Theory* **40**(7), 849–862 (2005).
7. C. Yang, Q. C. Li, Q. H. Chen and L. M. Xu, "Elastostatic stiffness modeling of overconstrained parallel manipulators," *Mech. Mach. Theory* **122**, 58–74 (2018).
8. B. Hu, Y. Lu, Q. Tan, J. P. Yu and J. D. Han, "Analysis of stiffness and elastic deformation of a 2(SP+SPR+SPU) serial-parallel manipulator," *Robot Comput. Integr. Manuf.* **27**(2), 418–425 (2011).
9. M. Gallant and C. Gosselin, "Singularities of a planar 3-RPR parallel manipulator with joint clearance," *Robotica* **36**(7), 1098–1109 (2018).
10. S. Venanzi and V. Parenti-Castelli, "A new technique for clearance influence analysis in spatial mechanisms," *J Mech. Design* **127**(3), 446–455 (2005).
11. M. Farajitabar, H. M. Daniali and S. M. Varedi, "Pick and place trajectory planning of planar 3RPR parallel manipulator in the presence of joint clearance," *Robotica* **35**(2), 241–253 (2017).
12. P. Flores, J. Ambrósio, J. C. P. Claro, H. M. Lankarani and C. S. Koshy, "A study on dynamics of mechanical systems including joints with clearance and lubrication," *Mech. Mach. Theory* **41**(3), 247–261 (2006).
13. T. N. Shiau, Y. J. Tsai and M. S. Tsai, "Nonlinear dynamic analysis of a parallel mechanism with consideration of joint effects," *Mech. Mach. Theory* **43**(4), 491–505 (2008).
14. S. M. Varedi-Koulaei, H. M. Daniali and M. Farajtabar, "The effects of joint clearance on the dynamics of the 3RRR planar parallel manipulator," *Robotica* **35**(6), 1223–1242 (2017).
15. L. X. Xu and Y. G. Li, "Investigation of joint clearance effects on the dynamic performance of a planar 2-DOF pick-and-place parallel manipulator," *Robot Comput. Integr. Manuf.* **30**(1), 62–73 (2014).
16. B. B. Lian, T. Sun, Y. M. Song, J. Yan and P. Mark, "Stiffness analysis and experiment of a novel 5-DoF parallel kinematic machine considering gravitational effects," *Int. J. Mach. Tools. Manuf.* **95**, 82–96 (2015).
17. A. Pashkevich, D. Chablat and P. Wenger, "Stiffness analysis of overconstrained parallel manipulators," *Mech. Mach. Theory* **44**(5), 966–982 (2009).
18. Y. Li and Q. Xu, "Stiffness analysis for a 3-PUU parallel kinematic machine," *Mech. Mach. Theory* **43**(2), 186–200 (2008).
19. S. R. Lim, K. Kang, S. Park, W. C. Choi, J. B. Song, D. Hong and J. K. Shim, "Error analysis of a parallel mechanism considering link stiffness and joint clearances," *Keme. Int. J.* **16**(6), 799–809 (2002).
20. M. Hafezipour and S. Khodaygan, "An uncertainty analysis method for error reduction in end-effector of spatial robots with joint clearances and link dimension deviations," *Int. J. Comput. Integ. M.* **30**(6), 653–663 (2017).
21. J. Aginaga, O. Altuzarra, E. Macho and X. Iriarte, "Assessing position error due to clearances and deformations of links in parallel manipulators," *J. Mech. Design* **135**(4), 1–8 (2013).
22. P. Flores, J. Ambrosio, J. C. P. Claro and H. M. Lankarani, "Dynamics of multibody systems with spherical clearance joints," *J. Comput. Nonlin. Dyn.* **1**(3), 240–247 (2006).
23. G. X. Wang and H. Z. Liu, "Dynamics model of 4-SPS/CU parallel mechanism with spherical clearance joint and flexible moving platform," *J. Tribol-T. ASME* **140**(2), 1–10 (2018).
24. Q. Tian, P. Flores and H. M. Lankarani, "A comprehensive survey of the analytical, numerical and experimental methodologies for dynamics of multibody mechanical systems with clearance or imperfect joints," *Mech. Mach. Theory* **122**, 1–57 (2018).

https://doi.org/10.1017/S0263574718001492 Published online by Cambridge University Press

25. J. Meng, D. J. Zhang and Z. X. Li, "Accuracy analysis of parallel manipulators with joint clearance," *J. Mech. Design* **131**(1), 1–9 (2009).
26. A. Frisoli, M. Solazzi, D. Pellegrinetti and M. Bergamasco, "A new screw theory method for the estimation of position accuracy in spatial parallel manipulators with revolute joint clearances," *Mech. Mach. Theory* **46**(12), 1929–1949 (2011).
27. A. Cammarata, "A novel method to determine position and orientation errors in clearance-affected overconstrained mechanisms," *Mech. Mach. Theory* **118**, 247–264 (2017).
28. H. Wang, L. S. Zhang, G. L. Chen and S. Z. Huang, "Parameter optimization of heavy-load parallel manipulator by introducing stiffness distribution evaluation index," *Mech. Mach. Theory* **108**, 244–259 (2017).
29. Y. Y. Wang, H. T Liu, T. Huang and D. G. Chetwynd, "Stiffness modeling of the Tricept robot using the overall Jacobian matrix," *J. Mech. Rob.* **1**(2), 1–8 (2009).
30. H. T. Liu, T. Huang and D. G. Chetwynd, "A general approach for geometric error modeling of lower mobility parallel manipulators," *J. Mech. Rob.* **3**(2), 1–13 (2011).
31. W. D. Wu and S. S. Rao, "Interval approach for the modeling of tolerances and clearances in mechanism analysis," *J. Mech. Design* **126**(4), 581–592 (2004).
32. M. Tannous, S. Caro and A. Goldsztejn, "Sensitivity analysis of parallel manipulators using an interval linearization method," *Mech. Mach. Theory* **71**, 93–114 (2014).
33. J. P. Merlet, "Interval analysis for certified numerical solution of problems in robotics," *Int. J. Ap. Mat.Com-Pol.* **19**(3), 399–412 (2009).
34. K. Luo and X. P. Du, "Probabilistic mechanism analysis with bounded random dimension variables," *Mech. Mach. Theory* **60**, 112–121 (2013).
35. S. S. Rao and P. K. Bhatti, "Probabilistic approach to manipulator kinematics and dynamics," *Reliab. Eng. Syst. Safe* **72**(1), 47–58 (2001).
36. X. P. Du, P. K. Venigella and D. S. Liu, "Robust mechanism synthesis with random and interval variables," *Mech. Mach. Theory* **44**(7), 1321–1337 (2009).
37. S. Fan and S. W. Fan, "An improved approach to the inverse dynamic analysis of parallel manipulators by a given virtual screw," *Adv. Rob.* **32**(16), 887–902 (2018).
38. V. L. Popov, *Contact Mechanics and Friction Physical Principles and Applications* (Springer, Berlin-Heidelberg, 2010).
39. S. M. Ross, *Simulation* (Fifth Edition). (Elsevier, Netherlands, 2013).

https://doi.org/10.1017/S0263574718001492 Published online by Cambridge University Press